Mechanics Research Communications 153 (2026) 104656

Contents lists available at ScienceDirect

Mechanics Research Communications

journal homepage: www.elsevier.com/locate/mechrescom

Mechanical behavior and wave-mitigation potential of metaconcretes with solidified/stabilized soil aggregates

Giuseppina Di Chiara [a,b,*], Marco Miniaci [c], Ilenia Farina [d], Antonella Petrillo [d], Raimondo Luciano [d], Fernando Fraternali [a]

[a] Department of Civil Engineering, University of Salerno, Italy
[b] Department of Civil Engineering and Architecture, University of Catania, Italy
[c] Dipartimento di Ingegneria Strutturale, Edile e Geotecnica, Politecnico di Torino, Italy
[d] Department of Engineering, University of Naples "Parthenope", Italy

ARTICLE INFO

Keywords:
Metaconcrete
Stabilization
Solidification
Experimental behavior
Bandgap response

ABSTRACT

This study investigates the mechanical response and wave attenuation performance of an innovative metaconcrete incorporating engineered aggregates composed of solidified/stabilized (S/S) contaminated soil encapsulated within a compliant polymeric coating. The proposed material integrates soil remediation strategies with the design of functional cement-based metamaterials, offering a sustainable solution for vibration and stress-wave mitigation. An experimental campaign was carried out to characterize the elastic properties of the examined stabilized soil, including Young's modulus and Poisson's ratio, through compression tests on cylindrical specimens. These experimentally measured properties were subsequently employed to inform both analytical modeling and finite element simulations aimed at predicting the dynamic behavior of the metaconcrete. Dispersion analyses based on Bloch–Floquet theory were performed on a representative unit cell to identify polarization-selective bandgaps associated with local resonance phenomena. The results reveal the presence of a well-defined longitudinal bandgap in the frequency range approximately between 6.5 and 7.5 kHz. A strong agreement is observed between analytical predictions and FEM-based dispersion curves, confirming the robustness of the adopted multiscale modeling framework. The numerical results further highlight the role of local resonance in promoting energy localization within the compliant coating, leading to a marked reduction in longitudinal wave propagation. Overall, the findings demonstrate that stabilized contaminated soils, when properly encapsulated, can be effectively repurposed as resonant inclusions in metaconcrete, combining environmental sustainability with advanced wave attenuation capabilities. The proposed metaconcrete formulation shows significant potential for applications in vibration mitigation, acoustic insulation, seismic shielding, and blast-resistant structural systems.

1. Introduction

A new class of metamaterials, referred to as *metaconcrete*, has been introduced in recent years [1,2]. This material is characterized by the replacement of traditional aggregates with engineered inclusions. Specifically, metaconcrete consists of spherical (or alternatively shaped) aggregates comprising a heavy metal core coated with a compliant material layer. A distinctive feature of this material is that, when excited at specific frequencies, the aggregates exhibit resonant behavior, oscillating about their equilibrium positions. As a result, a portion of the mechanical energy supplied to the system is effectively trapped within the inclusions. Due to its unique configuration, featuring embedded resonators, metaconcrete has demonstrated promising mechanical performance [3]. Moreover, non-destructive dynamic tests have revealed a significant reduction in the transmitted signal amplitude compared to conventional concrete, with the degree of attenuation depending on the type of inclusions and material properties [3,4]. Building on these observations, Chen et al [5] developed an analytical predictive model for designing locally resonant bandgaps, correlating the onset of the bandgap with the translational vibration mode of the resonator and the cutoff frequency with the coupling strength between the resonator and the matrix. Subsequent finite element simulations characterized the

* Corresponding author.
E-mail address: gdichiara@unisa.it (G. Di Chiara).

https://doi.org/10.1016/j.mechrescom.2026.104656
Received 2 January 2026; Received in revised form 11 February 2026; Accepted 19 February 2026
Available online 20 February 2026

bandgap regions and showed how variations in core size, coating thickness, and core density impact attenuation performance. This work also introduced a design flowchart to systematically guide the creation of metaconcrete with multiple resonance frequencies [6]. From an experimental perspective the authors demonstrated that metaconcrete can reduce maximum deformation by up to 72% compared to a homogeneous material, highlighting its potential for damage mitigation in structures subjected to dynamic loading [7]. Further studies reported in the literature have shown that metaconcrete-based barriers can effectively trap and convert surface elastic waves. Time-domain analyses based on real seismic recordings suggested that metaconcrete could be applied as a seismic shield to protect civil infrastructure from destructive events [8]. In 2024, Firhea et al [9] proposed the use of rubber aggregates with shielding capabilities to enhance the mechanical performance of metaconcrete, investigating wave attenuation at the mesoscale and strategies to optimize material behavior. The impact of aggregate shape on bandgap properties was studied in [10], while nacre-inspired mechanical metamaterials with "brick-and-mortar" architectures and potential applications in civil engineering were recently presented in [11, 12]. Furthermore, it has been demonstrated through a combined analytical with finite element approach that metaconcrete structures with engineered aggregates and appropriate boundary conditions offer a wider attenuation range and greater protection against stress wave propagation compared to conventional materials [13].

An innovative approach reported in the literature involves the use of contaminated soils treated through Solidification/Stabilization (S/S), yielding materials suitable for metaconcrete applications, as presented in [14]. In this context, the so-called *StabSoil MetaConcrete* (SSMC) was introduced as a novel strategy for reusing contaminated soils by transforming them into functional components of construction materials. Recent advances in stabilization processes have also enabled the incorporation of alternative binders to replace conventional cement [15], including pozzolanic compounds, fly ash (FA), rice husk ash [16], ground granulated blast furnace slag (GGBFS) [17–19], and bentonite [20]. The incorporation of these materials has enhanced both the efficiency and adaptability of the process, enabling its application across a broader range of contaminated sites. Partial replacement of Portland cement with alternative binders, characterized by lower energy consumption and reduced embodied carbon, significantly decreases the material's environmental footprint. These binders, often derived from industrial by-products such as fly ash or ground granulated blast furnace slag, offer environmentally friendly solutions. Their use in the stabilization of contaminated soils minimizes reliance on Portland cement while efficiently managing industrial waste and improving overall sustainability [21]. For instance, the substitution of Portland cement with eco-friendly alternative binders [22] results in a final material that is safe and free from risks to human health and the environment. The encapsulation of stabilized soil within a soft coating, which is then integrated into a cementitious matrix, allows contaminated soil to be safely incorporated into a composite material, preventing direct exposure to the surrounding environment. This process opens the way to new applications in civil engineering. In this context, the present work investigates the mechanical response and wave-propagation characteristics of an innovative type of metaconcrete, adopting a multichannel approach that combines experimental investigations, sample fabrication, analytical formulation, and theoretical analyses based on the finite element method. The paper is organized as follows. Section 2 provides a detailed description of the materials employed and the sample preparation procedure, highlighting the underlying design choices. Section 3 presents the mechanical tests performed, together with the corresponding results, to assess the performance characteristics of the materials. Section 4 outlines the analytical formulation, obtained by extending earlier studies [14] and grounded in the formulation introduced in [5], which is here integrated with the experimental data. Section 5 presents a finite element analysis aimed at further investigating the structural behavior and at comparing numerical predictions with the experimental findings. Section 6 discusses and compares the results, highlighting correlations, emerging trends, and practical implications. Finally, Section 7 summarizes the main conclusions of the study and outlines potential directions for future research.

2. Preparation of S/S samples

2.1. Material selection

In a previous study [14], three different mixtures composed of contaminated soil and stabilizing materials were developed. Specifically, the mixtures consist of soil, cement, GGBFS, and Municipal Solid Waste Incineration Fly Ash (MSWI-FA) in varying proportions, as detailed in Table 1. The soil, described thoroughly in [14], originates from industrial sites in the province of Naples and is contaminated with heavy metals and organic chemical compounds. Chemically, the sample contains significant concentrations of pollutants, including arsenic (72.0 mg/kg), cadmium (2.4 mg/kg), lead (37.3 mg/kg), and mercury (2.2 mg/kg), all of which are key indicators of contamination typically associated with industrial activities and known for their detrimental effects on soil quality and ecosystem health. The presence of nickel (28.9 mg/kg) and cobalt (6.0 mg/kg) further confirms the extent of heavy metal pollution.

Regarding the other materials used, the binder component is Portland cement CEM II/A-LL 42.5 R. The fly ash, derived from the incineration of municipal solid waste, was pre-treated through a washing process aimed at reducing the chloride and sulfate content; as a result, it is referred to as W-FA (Washed Fly Ash). Finally, the GGBFS was found to consist mainly of silicon, calcium, iron, and magnesium oxides, as revealed by previously conducted chemical analyses [15]. Among the mixtures developed, Mix 3 contains the highest proportion of contaminated soil (70%), thus enabling the solidification and stabilization of a larger volume of soil compared to the other formulations. This results in a higher overall density. For this reason, Mix 3 was selected for the present study, as specific gravity is considered a critical parameter for achieving the resonance effect generated by the internal core of the engineered aggregate. For the same reason, the mix design was enriched with tempered lead pellets No. 2/0, with an average measured diameter of 4.25 mm.

2.2. Preparation of cylindrical samples

Four specimens were prepared to analyze their mechanical properties. The specimens were manufactured in accordance with ASTM C192/C192M [23] and had a diameter of Ø 100 mm and a height of 200 mm. As previously mentioned, Mix Design 3 was used, with the mass percentages of its components shown in Table 1. Regarding the water content, a percentage of 16% relative to the total weight of the mixture was adopted. Table 2 presents the quantities, in grams, used for the preparation of each individual sample. The total weight of each mixture was 2.5 kg.

The materials were weighed and placed into a single container (Fig. 1) before being mixed using a mechanical mixer. First, all the dry materials were mixed together with water, and subsequently, the lead pellets were added, as described below.

All stages of the mixing process are shown in Fig. 2. Specifically,

Table 1
Percentage proportions of the StabSoil mixes considered in our previous studio [14].

	Mix 1	Mix 2	Mix 3
Cement	10	10	10
MSWI-FA	15	10	5
GGBFS	25	20	15
Soil	50	60	70

Table 2
Quantities of materials used for each sample.

	Amount	Units
Cement	0.250	kg
MSWI-FA	0.125	kg
GGBFS	0.375	kg
Soil	1.75	kg
Water	400	ml
Lead balls	2.18	kg

Fig. 1. Components before the mixing stage.

Fig. 2a displays all the materials inside the mixer, Fig. 2b illustrates the addition of the lead pellets, and Fig. 2c shows the final mix ready to be poured into cylindrical molds, with a close-up highlighting the presence of the lead pellets.

After the lead pellets were added, the mixture was poured into cylindrical steel molds, which had been previously treated with a form release agent, to produce the concrete specimens. Fig. 3 shows the molds filled with the mixture. The specimens were demolded after 48 h and then cured in a controlled environment (temperature and humidity) for 28 days prior to testing (Fig. 3b).

3. Mechanical testing of S/S soil samples

3.1. Experimental set up

To determine the elastic modulus (E) and Poisson's ratio (ν), ASTM standard C469/C469M [24] was followed, with appropriate adaptations for the use of strain gauges. According to this standard, specimens can be tested at different curing ages, such as 24 h, 3 days, 7 days, 28 days, and 90 days. In this study, the specimens were tested after 28 days of curing. The tests were carried out at the STRENGTH – STRuctural ENGineering Test Hall laboratory of the University of Salerno. The testing machine used was an electromechanical universal testing machine, model Quasar 400, serial number VFGA (2024), supplied by Cesare Galdabini S.p.A. It was equipped with a load cell with a maximum capacity of 750 kN, model TCA, serial number 251843, with an accuracy class of 0.5 in accordance with UNI EN ISO 7500-1:2018. An automatic contact extensometer, model Micron XT, serial number 35120, with an accuracy class of 0.5 according to UNI EN ISO 9513:2013, was also used. The machine was operated using the LABTEST 4.0 v.P control software, developed by Cesare Galdabini S.p.A. According to the procedure, one specimen must first undergo compression testing following ASTM C39/C39M [25] to determine the failure load. Subsequently, the main test can be performed on the other specimens equipped with strain gauges, allowing the calculation of the mechanical parameters involved. The Fig. 4 shows the experimental set up.

Each specimen was instrumented with 6 strain gauges, three vertical and three horizontal pairs, as shown in Fig. 5. The strain gauges used were model PL-60-11-3LJCT-F, manufactured by Tokyo Measuring Instruments Lab. They were 60 mm long, mounted on a polyester resin backing, and had a nominal resistance of 120 Ω.

The strain gauges were bonded following the standard procedure: first, the surface was cleaned, then prepared for bonding, and finally the strain gauges were glued in place. After this, the tests were carried out. As previously mentioned, an auxiliary specimen (without strain gauges) was tested first to determine the failure strength, since the standard required performing a cyclic test up to 40% of the maximum load. The test to determine the elastic modulus and the Poisson ratio is a load-controlled compression test, where the load is applied at a constant rate of 250kPa/s, gradually increasing to measure both longitudinal and transverse deformations. For the execution of the compression test, the ASTM C469/C469M standard [24] was followed, which includes the following steps: (1) Equip the sample with strain gauges; (2) Positioning of the specimen on the testing machine and align the specimen's axis with the center of thrust of the spherically seated upper bearing block; (3) Apply a preload of 0.5 MPa, then initiate the test by performing three loading–unloading cycles between the preload level and 40% of the estimated ultimate load. After these cycles, the specimen was loaded to failure. In accordance with the standard previously mentioned, the first cycle is intended to ensure proper alignment of the specimen, while the second and third cycles are used to determine the mechanical parameters. These were calculated by averaging the values obtained during the second and third loading ramps at two specific points: (1) the applied

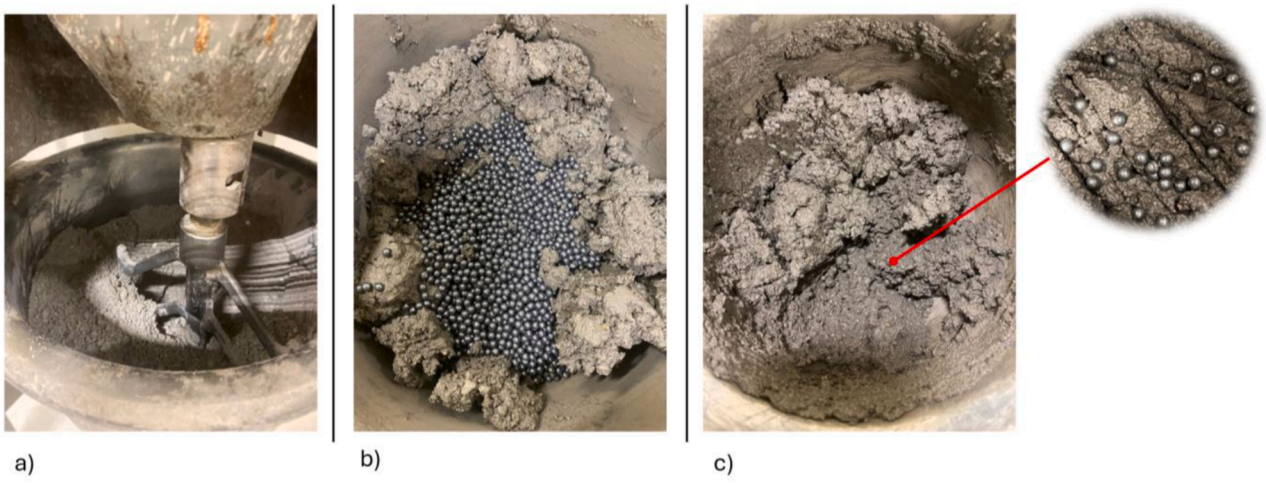

Fig. 2. Mixing process stages. a) photo of the mixer in operation; b) addition of lead pellets to the mixture; c) photo of the mixture after the addition of lead pellets.

Fig. 3. a) Freshly cast stabsoil specimens in cylindrical molds; b) curing of stabsoil specimens.

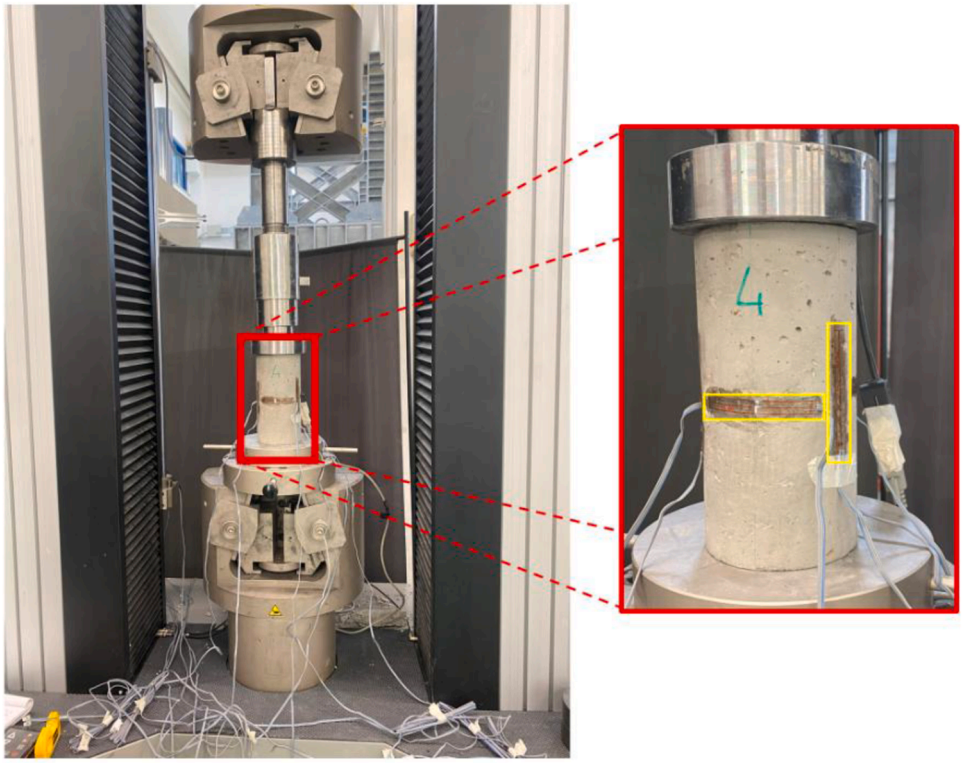

Fig. 4. Experimental set-up showing a cylindrical specimen in the testing machine and the spatial representation of the strain gauges.

load and corresponding longitudinal strain at 50 με, and (2) the load corresponding to 40% of the ultimate load. Centering the specimen proved particularly challenging due to the nature of the material. To avoid compromising its structural integrity, the initial preload was reduced to 0.3 MPa. This decision was based on the observation that the originally intended preload of 0.5 MPa caused initial strains exceeding 50 με. Nevertheless, the reference strain at low load was taken as 80 microstrain.

Then, using the obtained stress-strain curve, all the necessary parameters for calculating the elastic modulus is determined as follows:

$$\mathrm{E} = \frac{(S_2 - S_1)}{(\varepsilon_2 - 0.000080)} \tag{1}$$

where:

S_2 stress corresponding to 40% of ultimate load

S_1 stress corresponding to a longitudinal strain, ε_1, of 80 millionths

ε_2 longitudinal strain produced by stress S_2

While the Poisson's ratio is calculated using the following formula:

$$\mu = \frac{(\varepsilon_{t2} - \varepsilon_{t1})}{(\varepsilon_2 - 0.000080)} \tag{2}$$

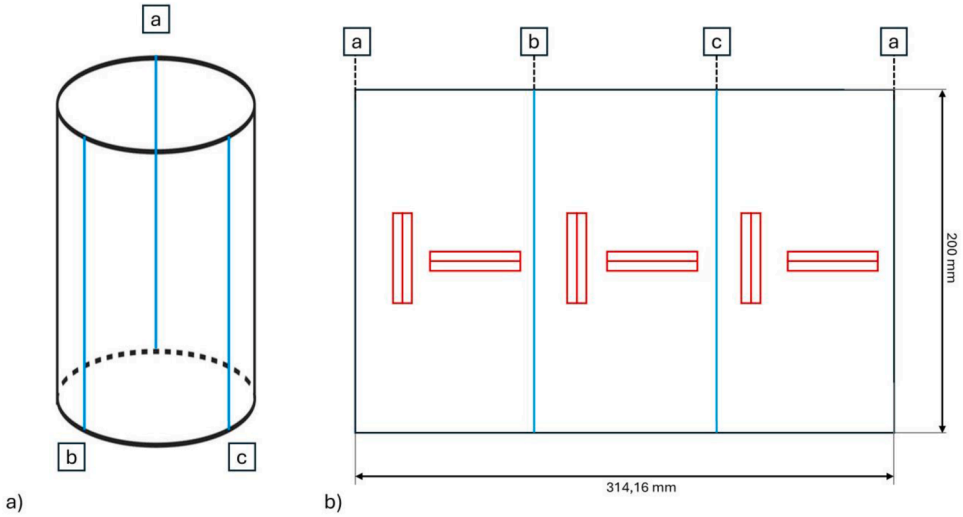

Fig. 5. Placement of the strain gauges over the cylindrical wall: a) 3D visualization; b) side projection.

Where

εt_2 transverse strain at midheight of the specimen produced by stress S_2

εt_1 transverse strain at midheight of the specimen produced by stress S_1.

3.2. Results

As mentioned previously, the first test was carried out on an auxiliary specimen to determine the compressive strength of the examined material, yielding a value of 5.8 MPa. This value was adopted as the initial reference for the subsequent experimental phase, during which compression tests were conducted on three additional specimens. Fig. 6 provides a focused analysis of the elastic region of the mechanical response observed in three cylindrical specimens #2, #3, #4. The data are derived from measurements acquired using strain gauges oriented both longitudinally and transversely to the loading axis. As observed in the graph, the curves diverge from the origin, revealing two simultaneous physical behaviors. In the left quadrant, vertical shortening is observed, with negative strains reaching approximately −800 μe at a maximum stress of 2.5 MPa; conversely, the right quadrant shows horizontal elongation. This circumferential expansion, although limited in magnitude (up to about +150 μe), clearly reflects the Poisson effect induced by axial loading. The evolution of the curves also reveals slight mechanical hysteresis between the loading and unloading phases and highlights the greater relative stiffness of specimen #4 compared with specimens #2 and #3. Furthermore, the vertical shortening and horizontal elongation curves appear close to each other and clearly distinguishable, with minimal dispersion. This indicates a good consistency in the strain gauge response, despite the high porosity of the specimens. The material's internal heterogeneity is also suggested by the lack of symmetry of the curves with respect to the origin, an expected behaviour in highly porous or non-homogeneous materials. Moreover, a slight nonlinearity is noticeable in the initial part of some curves, particularly during the first loading cycle. This behaviour can likely be attributed to imperfect specimen alignment during the setup phase, as previously discussed.

The graph highlights the vertical compression and horizontal elongation of the three specimens, which are critical for evaluating the elastic parameters. These measurements form the basis for calculating the Young's modulus (E) and the Poisson's ratio (ν). The complete results of the compression tests, including the full stress–strain curves up

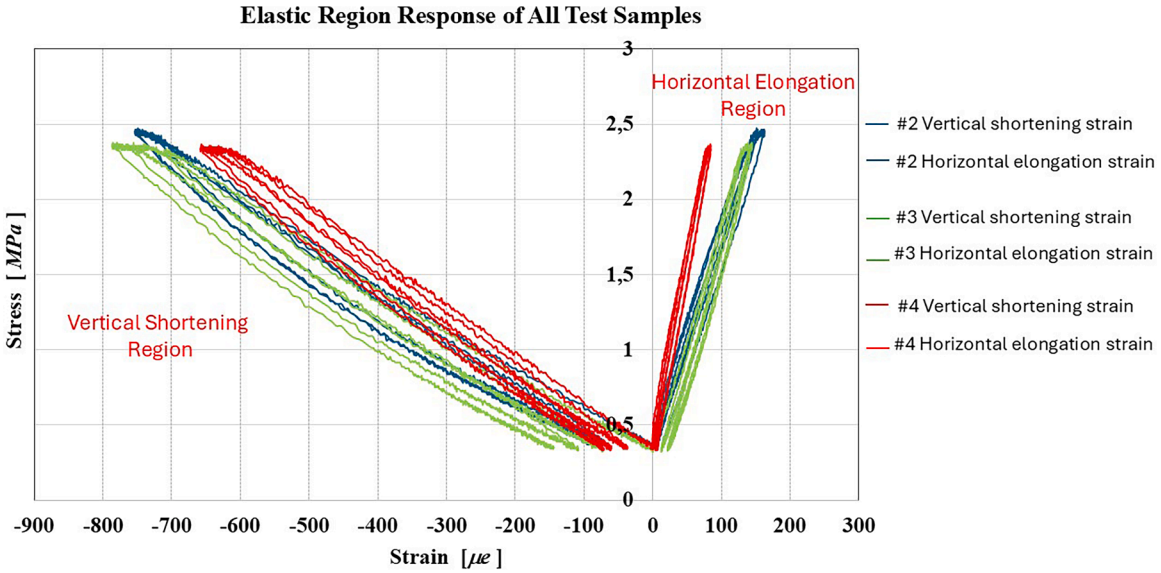

Fig. 6. Stress – strain curve of elastic region.

to failure, are presented in Fig. 7. is organized into three distinct panels:

- The left panel shows an image of the specimen placed in the testing press prior to the start of the experiment, documenting the initial test conditions.
- The central panel displays the full stress–strain curve, allowing a detailed analysis of the material's mechanical behaviour up to failure.
- The right panel presents a magnified view of the elastic region of the curve, from which the key mechanical parameters, Young's modulus (E) and Poisson's ratio (ν), were derived and shown in Table 3.

Furthermore, the comparison across the three specimens highlights a high degree of repeatability in both peak strength (approximately 6–7 MPa) and elastic slopes, confirming the material's homogeneity. The photographic insets document a typically brittle failure mode characterized by longitudinal fractures, which correlates with the rapid post-peak softening phase observed in the complete stress–strain curves.

4. Analytic formulation of the bandgap response

The present section summarizes the main results of the analytical formulation of the bandgap response of a one-dimensional strip composed of metaconcrete unit cells, which are discussed in detail in [6, 14]. The analysis illustrates how the system's bandgap evolves in response to key geometric parameters, including the unit cell length, core size, and coating thickness. The analytical model predicts that mechanical waves with a frequency f falling within the bandgap interval $[f_1, f_2]$ are unable to propagate through the rod. The lower bound f_1 corresponds to the onset of a purely translational motion of the resonator, with the surrounding matrix remaining theoretically stationary. Conversely, the upper cutoff frequency f_2 marks the initiation of relative motion between the resonator and the matrix, beyond which wave propagation becomes possible again. This concept was thoroughly addressed in our previous work [14], building upon the formulation introduced in 2023 [5] where the cutoff frequencies are expressed as:

$$f_1 = \frac{1}{2\pi}\sqrt{\frac{k}{m_1}} \tag{3}$$

$$f_2 = \frac{1}{2\pi}\sqrt{\frac{k(m_1+m_2)}{m_1 m_2}} \tag{4}$$

Here, m_1 and m_2 represent the equivalent (homogenized) masses of the resonator and the matrix, respectively, while k is the equivalent stiffness coefficient of the soft coating. By applying these expressions, the cutoff frequencies are found to be $f_1 = 6681.02$ Hz and $f_2 = 7823.49$ Hz. These analytical predictions will be compared and critically discussed against the finite element simulations presented in the following section.

5. Finite element-based dispersion analysis of the proposed metaconcrete

We illustrate hereafter the application of the Finite Element (FE) method to numerically predict the dispersion curves of a one-dimensional metaconcrete strip. A FE model of the representative unit cell is developed in COMSOL Multiphysics (see Fig. 8) to identify the potential emergence of frequency bandgaps (BGs), namely frequency ranges in which the propagation of elastic waves is inhibited. The influence of the mechanical properties of the solidified/stabilized soil aggregates and of the surrounding matrix on the dispersion characteristics is examined, and the numerical outcomes are discussed in relation to the experimentally measured material parameters.

Fig. 8 presents a schematic overall (left panel) and transversal cut (right panel) of the representative unit cell adopted as the fundamental geometry for the numerical simulations, capturing the essential features of the periodic structure of the metaconcrete. It consists of a cubic geometry with side length of $a = 35$ mm. The radius of the internal core composed of a solidified/stabilized soil is $r_1 = 10$ mm. This core is surrounded by a compliant coating of 2 mm of thickness, implying an external radius of the coating equals to $r_2 = 12$ mm. The physical and mechanical properties assigned to the different material phases, derives from the experimental characterization, are summarized in Table 4.

To compute the dispersion diagram of the proposed metaconcrete, an eigenfrequency analysis is performed assuming the unit cell to be infinitely periodic along the x-direction only. Accordingly, Bloch–Floquet periodic boundary conditions are applied to the opposite faces of the representative unit cell normal to the direction of periodicity, while the remaining boundaries are left traction-free. This formulation enables the modelling of elastic wave propagation in an unbounded periodic medium. Under these assumptions, the resulting generalized eigenvalue problem reads:

$$(\boldsymbol{K} - \omega^2 \boldsymbol{M})\boldsymbol{u} = 0 \tag{5}$$

where $\boldsymbol{K}$ and $\boldsymbol{M}$ denote the stiffness and mass matrices, respectively, and ω represents the angular frequency. The eigenvalue problem is solved using the PARDISO built-in solver available in COMSOL Multiphysics. Numerical convergence is ensured adopting a maximum finite element size equal to 6.7 mm, which guarantees accurate results up to the highest frequency of interest [26].

Following standard procedures for periodic media, the dispersion curves (reported in the top panel of Fig. 9) are obtained by sweeping the normalized wave vector $k^* = \boldsymbol{k_x}\frac{\pi}{a}$ (with, $k^* \epsilon [0,1]$) along the boundary of the first irreducible Brillouin zone. To determine the dominant displacement character of each eigenmode found through this procedure, a polarization coefficient $\boldsymbol{p}$, defined as follows:

$$\boldsymbol{p} = \frac{\int_V (|\boldsymbol{u_x}|)^2 \boldsymbol{dV}}{\int_V \left(|\boldsymbol{u_x}|^2 + |\boldsymbol{u_y}|^2 + |\boldsymbol{u_z}|^2\right)\boldsymbol{dV}}, \tag{6}$$

is calculated. In Eq. (6), V denotes the volume of the unit cell, $\boldsymbol{u_x}$, $\boldsymbol{u_y}$ and $\boldsymbol{u_z}$ the displacement components along x-, y- and z- directions, respectively. This approach builds on the methodology presented in Refs [27, 28] for separating in-plane and out-of-plane deformation components of the eigenmodes of phononic slab dispersion diagrams, and is here adapted to identify longitudinal displacement contributions in the considered metaconcrete unit cell. In fact, the polarization parameter $\boldsymbol{p}$ considered here, as defined in Eq. (6) identifies the ratio between the energy associated with the displacement component $\boldsymbol{u_x}$and the total displacement energy. This allows us to distinguish between longitudinal modes along the $\boldsymbol{x}$-axis from other types of modes where the displacements are mainly lying in the (y,z) plane. Specifically, values of $\boldsymbol{p} \approx 1$ identify modes that are strongly longitudinally polarized, i.e., the displacement energy is predominantly aligned with the direction of periodicity (see mode shapes in bottom panel of Fig. 9), whereas values of $\boldsymbol{p} \approx 0$ correspond to modes whose motion is predominant in the orthogonal plane.

The resulting dispersion relations are reported in the top panel of Fig. 9. For the sake of clarity, only the first two longitudinal modes are reported and labeled as L1 and L2. The corresponding mode shapes M1 and M2, shown in the bottom left panel of Fig. 9, clearly indicate that both modes are longitudinal in their nature. Modes characterized by a different polarization, although present within this frequency range, are not reported here as they do not affect the mechanism of the longitudinal BG opening. This simplified diagram allows us to immediately identify the presence of a BG for longitudinal waves in the frequency range between approximately 6500 Hz and 7500 Hz. Within this interval, no modes with significant $\boldsymbol{u_x}$ content are observed, confirming that the proposed metaconcrete unit cell can effectively suppresses longitudinal propagation along the $\boldsymbol{x}$-direction.

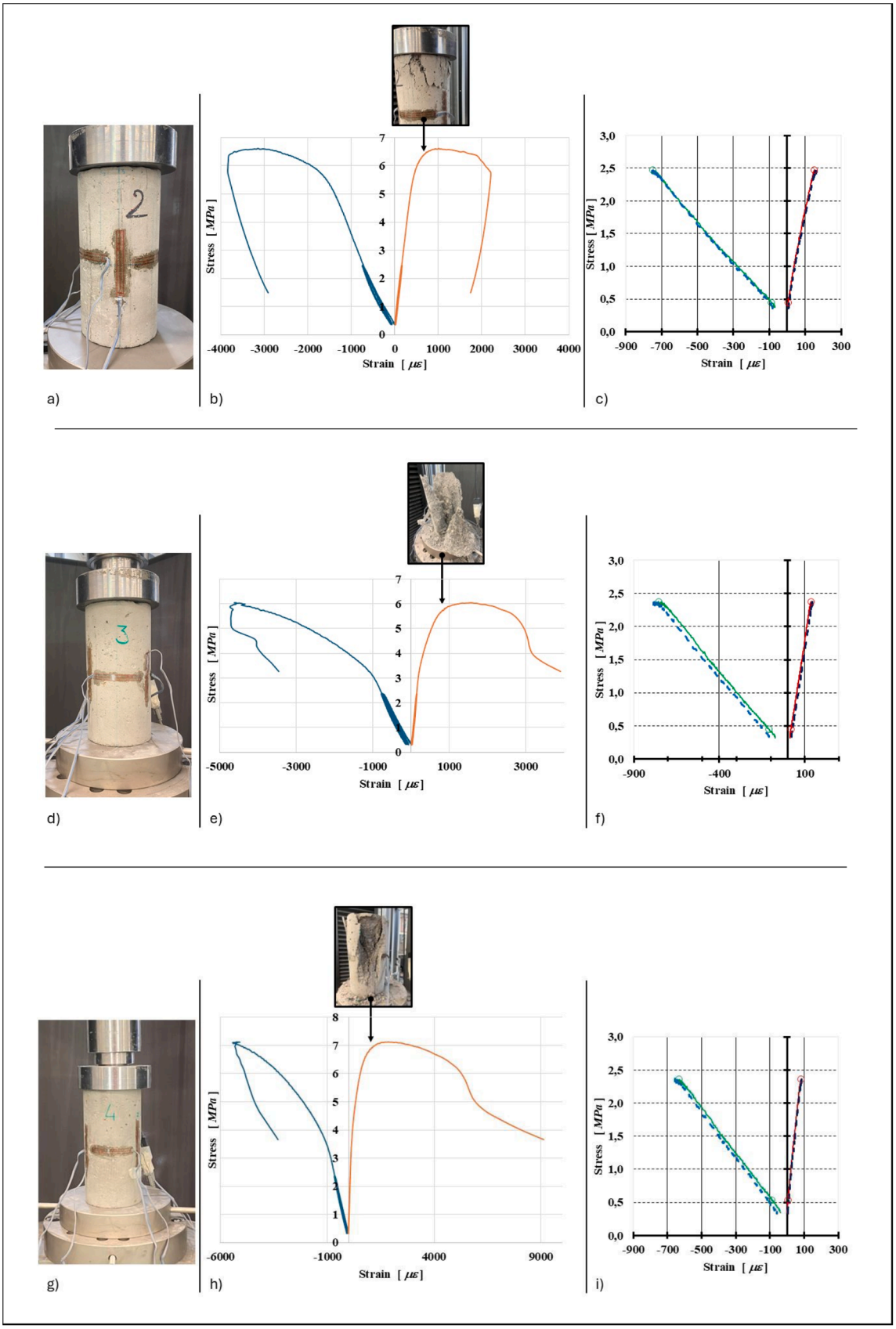

Fig. 7. Compression test on specimen #2, #3, #4.

Table 3
Summary of the investigated mechanical parameters.

Specimen	Failure (MPa)	Young's modulus (GPa)	Poisson ratio
#1	5.8	-	-
#2	6.63	3.11	0.23
#3	6.03	3.02	0.18
#4	7.11	3.36	0.14

To further corroborate these numerical findings, the locally resonant behavior responsible for energy localization and bandgap formation is compared with the experimental observations reported in [29], where bi-material inclusions composed of a metallic core and a polymeric coating were investigated. In full agreement with those experimental results, when the metaconcrete is excited at frequencies close to the eigenfrequencies of the inclusions, vibrational energy is preferentially trapped within the compliant coating (see mode shapes M3 and M4 in Fig. 9), leading to the opening of the BG, and thus to a marked reduction in wave transmissibility. The finite element simulations therefore reproduce the same physical phenomenology observed in dynamic tests, capturing the spatial localization of displacement fields that experimentally manifests as strong attenuation of stress waves at the resonant frequencies of the inclusions.

6. Discussion: comparison of analytic and FEM results

The analytical results presented in Section 3, derived from the formulation proposed in [5], predict the emergence of a bandgap with a width of approximately 1150 Hz, bounded by a lower frequency $f_1 = 6681.02$ Hz and an upper cut-off frequency $f_2 = 7823.49$ Hz. This attenuation interval is of particular significance as it confirms the capability of the analytical model to accurately capture the dynamic response of the metaconcrete system. The excellent agreement with the numerical results obtained through FEM simulations in COMSOL, discussed in the previous section, further validates the theoretical formulation. Indeed, both approaches converge toward a consistent description of the bandgap phenomenon, with only negligible discrepancies. This strong correspondence is clearly illustrated in Fig. 10, which shows an almost perfect overlap between the analytically predicted and numerically computed bandgap boundaries.

The bandgap identified in the present study, spanning approximately from 6.6 to 7.8 kHz, is in good agreement with findings reported in the literature, although some variations can be observed due to differences in material composition, geometric configuration, and loading conditions. A meaningful comparison can be drawn with the experimental study by Kettenbeil and Ravichandran [8], who reported an attenuation interval between 10 and 15 kHz in metaconcrete systems featuring spherical inclusions coated with a polymeric layer. While the absolute frequency range differs, the underlying physical mechanism remains consistent: in both cases, the bandgap originates from local resonance effects associated with the generation of a negative effective mass beyond the resonant frequency of the inclusions (see Fig. 10).

Further insight is provided by more recent simulations reported in Ref [9], which identified an initial bandgap in the range 6.8–9.3 kHz, near the analytical predictions obtained in the present work. In that study, the introduction of rubber aggregates and viscoelastic dissipation mechanisms resulted in a substantial broadening of the attenuation window, extending it up to 16.3 kHz and increasing the bandgap width by more than 50%. Complementary evidence is offered by Xu et al [30], who demonstrated that the adoption of advanced engineered inclusions combined with the inclusion of equivalent shear stiffness effects enables a downward shift of the attenuation region and the emergence of multiple bandgaps across both low- and high-frequency regimes.

The overall agreement with these studies confirms the robustness of the theoretical framework rooted in the formulation by Milton and Willis [2]. Nevertheless, some limitations remain, particularly those related to scale effects and material selection. In the present case, the bandgap is in a mid-frequency range, which is consistent with the elastic properties and geometric parameters of the modelled system.

Table 4
Physical and mechanical properties of the unit cell.

Property	Soft coating	Matrix	StabSoil core
Density (kg/m^3)	1220	1000	2600
Young's modulus (Pa)	1×10^7	1×10^{10}	1×10^9
Poisson ratio	0.48	0.2	0.18

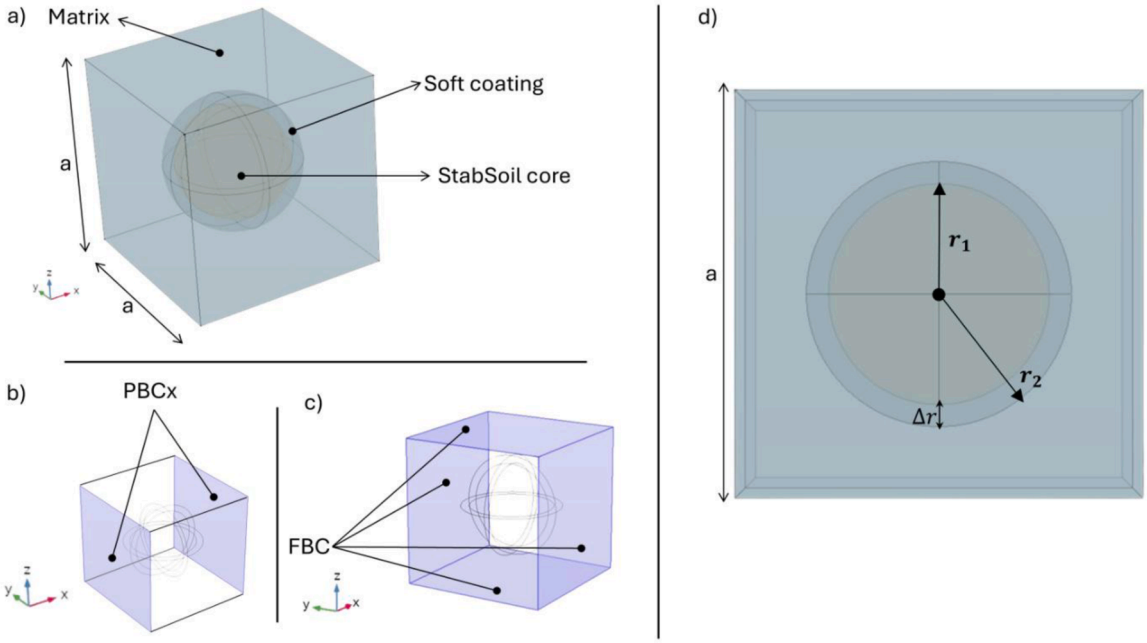

Fig. 8. Schematic representation of the unit cell adopted in COMSOL FEM analysis. Acronyms "PBC" and "FBC" indicate "periodic boundary conditions" and "free boundary conditions", respectively.

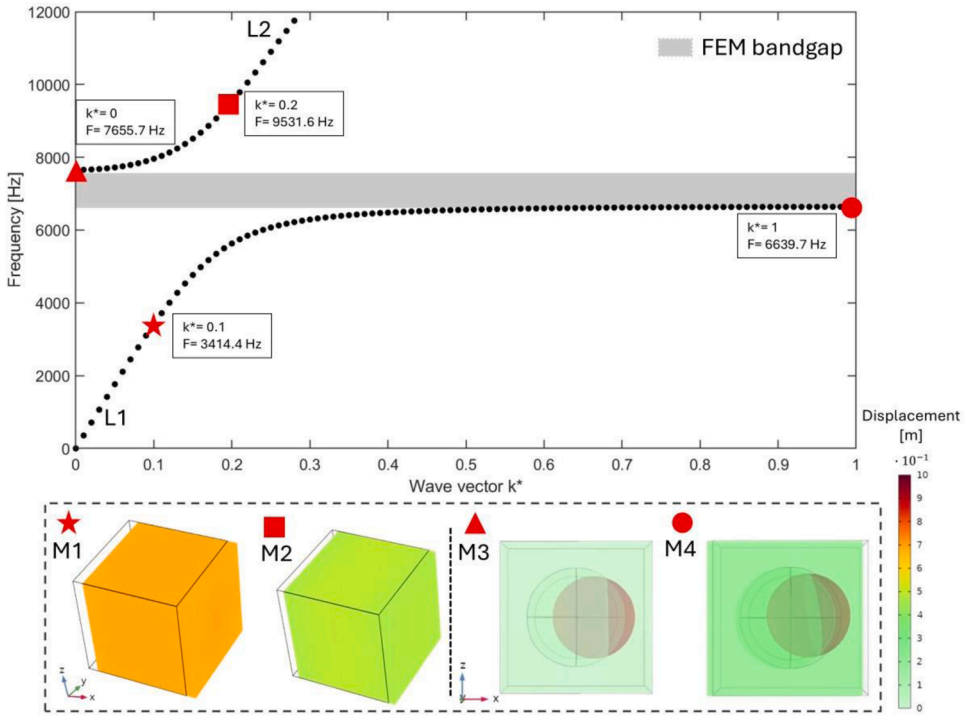

Fig. 9. Band diagram of the metaconcrete unit cell subjected to periodicity along the x-axis and relevant mode shapes. (Top panel) A polarization-selective bandgap for longitudinal waves is observed in the frequency range approximately between 6500 and 7500 Hz. In this frequency range, highlighted as a grey rectangle, no modes with dominant displacement along the x-direction are present. (Bottom panel) Relevant mode shapes showing the longitudinal polarization of the displacement of the reported curves (M1 and M2), as well as mode shapes at the bottom and top boundaries of the BG (M3 and M4), revealing a strong localization of the deformation inside the rubber coating. Transverse modes appearing within the same frequency interval are not affected by the bandgap mechanism and are therefore not considered in the present analysis (not reported in the band diagram).

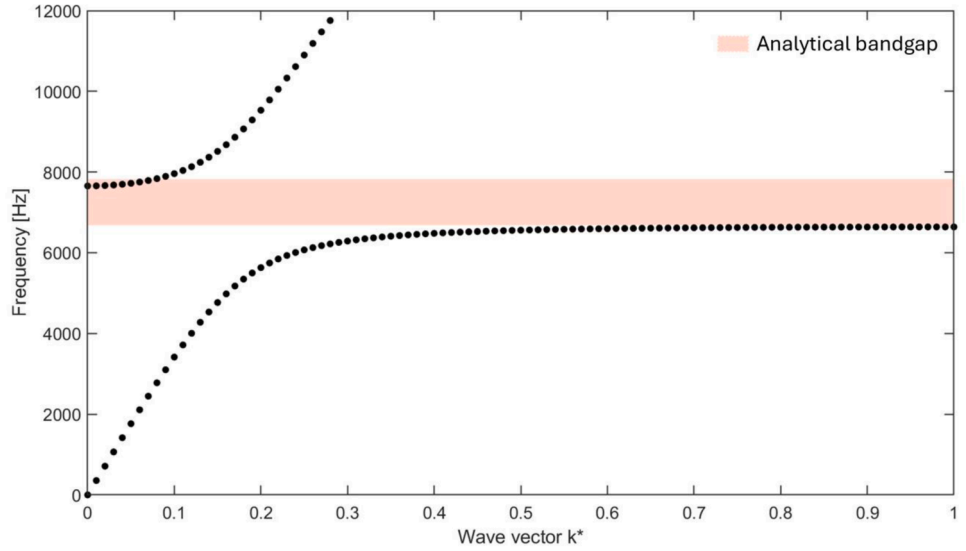

Fig. 10. Comparison between analytical predictions and FEM simulations, highlighting the bandgap region.

7. Concluding remarks

This study has investigated the mechanical response and wave attenuation capabilities of an innovative metaconcrete formulation incorporating engineered aggregates composed of solidified/stabilized contaminated soil encapsulated within a compliant polymeric coating. The proposed StabSoil MetaConcrete represents a novel and sustainable approach that integrates soil remediation strategies with the design of functional metamaterials for civil engineering applications. An experimental campaign was first conducted to characterize the mechanical properties of the stabilized soil, yielding reliable estimates of Young's modulus and Poisson's ratio. These experimentally derived parameters were subsequently employed to inform both analytical modeling and finite element simulations aimed at predicting the dynamic response of the metaconcrete. The combined analytical–numerical framework enabled the identification of a well-defined, polarization-selective bandgap for longitudinal elastic waves in the frequency range approximately between 6.5 and 7.5 kHz.

A remarkable agreement was observed between analytical predictions and FEM-based dispersion analyses, with an almost perfect overlap of the bandgap boundaries. This consistency confirms the robustness of the adopted modeling strategy and validates the use of experimentally characterized material properties for bandgap prediction. The numerical results further revealed that the attenuation mechanism is governed by local resonance phenomena, leading to pronounced energy localization within the compliant coating of the engineered inclusions. Comparison with existing literature demonstrated strong convergence with previous experimental and numerical studies on metaconcrete systems, while also highlighting the critical role of material selection and microstructural configuration in determining the position and width of the attenuation region. In parallel with these developments, recent studies have explored the use of unconventional aggregates and composite inclusions to tailor both the mechanical response and the dynamic behavior of cementitious materials. In particular, the work of [31] demonstrated that engineered aggregate–matrix interactions can significantly influence stiffness, damage evolution, and energy dissipation mechanisms, further supporting the potential of aggregate-based metamaterial concepts in civil engineering applications. Within this context, the specific the use of stabilized soil as the resonant core introduces an additional degree of freedom for tuning the dynamic response, while simultaneously promoting environmentally sustainable construction practices. Overall, this work contributes to the growing body of research on metaconcrete by demonstrating that contaminated soils, once properly stabilized and encapsulated, can be effectively repurposed as functional resonant inclusions in advanced cement-based metamaterials. Future developments should focus on extending the attenuation window toward lower frequencies through optimized inclusion geometries, multi-resonator configurations, and the incorporation of highly dissipative or viscoelastic materials, thereby further enhancing the applicability of metaconcrete for vibration mitigation, seismic shielding, and blast-resistant structural systems.

Funding

This work was supported by the National Recovery and Resilience Plan (NRRP), Mission 4, Component 2, Investment 1.1, Call for tender No. 1409 published on 14.9.2022 by the Italian Ministry of University and Research (MUR), funded by the European Union – NextGenerationEU – Project title: 'Stabilization of contaminated soils' (STABSOIL) – P2022CR8AJ – CUP D53D23018180001 (A.P. PI). It has also been supported by the National Recovery and Resilience Plan (NRRP), Mission 4, Component 2, Investment 1.1, Call for tender No. 104 published on 2.2.2022 by the Italian Ministry of University and Research (MUR), funded by the European Union – NextGenerationEU – Project title 'Innovative tensegrity lattices and architectured metamaterials' (ILAM) – 20224LBXMZ – CUP D53D23003020006 (F.F. PI). F.F. also acknowledges support by the Italian Ministry of Foreign Affairs and International Cooperation within the Italy-USA Science and Technology Cooperation Program 2023–2025, Project 'Next-generation green structures for natural disaster-proof buildings', grant number US23GR15. G.D.C. thanks the Italian Dottorato di Interesse Nazionale 'Defense against Natural Risks and Ecological Transition of Built Environment'. M.M. acknowledges the DREAM project that received funding from the European Union Next-GenerationEU (National Recovery and Resilience Plan – NRRP, Mission 4, Component 2, Investment 1.2).

CRediT authorship contribution statement

Giuseppina Di Chiara: Writing – review & editing, Writing – original draft, Validation, Software, Methodology, Investigation, Formal analysis, Data curation, Conceptualization. **Marco Miniaci:** Writing – review & editing, Writing – original draft, Validation, Software, Methodology, Investigation, Conceptualization. **Ilenia Farina:** Writing – original draft, Resources, Investigation. **Antonella Petrillo:** Writing – review & editing, Writing – original draft, Funding acquisition. **Raimondo Luciano:** Writing – original draft, Investigation. **Fernando Fraternali:** Writing – review & editing, Writing – original draft, Supervision, Methodology, Funding acquisition, Data curation.

Declaration of competing interest

The authors declare that they have no known competing financial interests or personal relationships that could have appeared to influence the work reported in this paper.

Acknowledgements

The authors gratefully acknowledge the support received by Gerardo Carpentieri (Department of Civil Engineering, University of Salerno) in the development of the numerical simulations.

Data availability

Data will be made available on request.

References

[1] S.J. Mitchell, A. Pandolfi, M. Ortiz, Metaconcrete: designed aggregates to enhance dynamic performance, J. Mech. Phys. Solids. 65 (2014) 69–81, https://doi.org/10.1016/j.jmps.2014.01.003.
[2] G.W. Milton, J.R. Willis, On modifications of Newton's second law and linear continuum elastodynamics, Proc. R. Soc. Math. Phys. Eng. Sci. 463 (2079) (2007) 855–880, https://doi.org/10.1098/rspa.2006.1795.
[3] D. Briccola, M. Ortiz, A. Pandolfi, Experimental validation of metaconcrete blast mitigation properties, J. Appl. Mech. 84 (3) (2017) 031001. doi:10.1115/1.4035259.
[4] D. Briccola, A. Pandolfi, Analysis on the dynamic wave attenuation properties of metaconcrete considering a quasi-random arrangement of inclusions, Front. Mater. 7 (2021), https://doi.org/10.3389/fmats.2020.615189.
[5] J. Chen, X. Zeng, H.A. Umar, Y. Xie, G. Long, Research on vibration reduction performance of metaconcrete based on local resonance theory, J. Build. Eng. 71 (2023) 106520, https://doi.org/10.1016/j.jobe.2023.106520.
[6] C. Xu, W. Chen, H. Hao, H. Jin, Effect of engineered aggregate configuration and design on stress wave attenuation of metaconcrete rod structure, Int. J. Solids. Struct. 232 (2021) 111182, https://doi.org/10.1016/j.ijsolstr.2021.111182.
[7] Z. Chen, G. Wang, C.W. Lim, Artificially engineered metaconcrete with wide bandgap for seismic surface wave manipulation, Eng. Struct. 276 (2023) 115375, https://doi.org/10.1016/j.engstruct.2022.115375.
[8] C. Kettenbeil, G. Ravichandran, Experimental investigation of the dynamic behavior of metaconcrete, Int. J. Impact. Eng. 111 (2018) 199–207, https://doi.org/10.1016/j.ijimpeng.2017.12.008.
[9] A. Fireha, R. Zhou, Y. Liu, L.G. Wang, W. Wang, J. Wang, Mesoscale modelling of metaconcrete containing rubber aggregates towards wave attenuation against impact loadings. case studies in construction, Materials 20 (2024) e03127, https://doi.org/10.1016/j.cscm.2024.e03127.
[10] C. Xu, W. Chen, H. Hao, The influence of design parameters of engineered aggregate in metaconcrete on bandgap region, J. Mech. Phys. Solids. 139 (2020) 103929, https://doi.org/10.1016/j.jmps.2020.103929.
[11] A. Pranno, F. Greco, L. Leonetti, P. Lonetti, R. Luciano, U. De Maio, Band gap tuning through microscopic instabilities of compressively loaded lightened nacre-like composite metamaterials, Compos. Struct. 282 (2022) 115032, https://doi.org/10.1016/j.compstruct.2021.115032.
[12] U. De Maio, F. Greco, R. Luciano, G. Sgambitterra, A. Pranno, Microstructural design for elastic wave attenuation in 3D printed nacre-like bioinspired metamaterials lightened with hollow platelets, Mech. Res. Commun. 128 (2023) 104045, https://doi.org/10.1016/j.mechrescom.2023.104045.
[13] C. Xu, W. Chen, T.M. Pham, K. Bi, R. Cheng, H. Hao, Designing novel metaconcrete structures with low-frequency bandgap against dynamic loads, Structures 70 (2024) 107748, https://doi.org/10.1016/j.istruc.2024.107748.
[14] A. Petrillo, G. Di Chiara, A. Acampora, F. Fraternali, I. Farina, Application of stabilized contaminated soils as metaconcrete aggregates, Meccanica (2025), https://doi.org/10.1007/s11012-025-01999-z.
[15] A. Petrillo, F. Fraternali, A. Acampora, G. Di Chiara, F. Colangelo, I. Farina, Innovative solidification and stabilization techniques using industrial by-products for soil remediation, Appl. Sci. 15 (7) (2025) 4002, https://doi.org/10.3390/app15074002.
[16] C.Y. Yin, H. Mahmud, M. Shaaban, Stabilization/solidification of lead-contaminated soil using cement and rice husk ash, J. Hazard. Mater. 137 (2006) 1758–1764, https://doi.org/10.1016/j.jhazmat.2006.05.013.
[17] H. Wang, Z. Zhu, S. Pu, W. Song, Solidification/stabilization of Pb2+ and Cd2+ contaminated soil using fly ash and GGBS based geopolymer, Arab. J. Sci. Eng. 47 (4) (2022) 4385–4400, https://doi.org/10.1007/s13369-021-06109-1.

[18] E. Özbay, M. Erdemir, H.İ. Durmuş, Utilization and efficiency of ground granulated blast furnace slag on concrete properties–a review, Constr. Build. Mater. 105 (2016) 423–434, https://doi.org/10.1016/j.conbuildmat.2015.12.153.
[19] S. Teng, T.Y.D. Lim, B. Sabet Divsholi, Durability and mechanical properties of high strength concrete incorporating ultra fine ground granulated blast-furnace slag, Constr. Build. Mater. 40 (2013) 875–881, https://doi.org/10.1016/j.conbuildmat.2012.11.052.
[20] Y. Mao, F. Muhammad, L. Yu, M. Xia, X. Huang, B. Jiao, Y. Shiau, D. Li, The solidification of lead-zinc smelting slag through bentonite supported alkali-activated slag cementitious material, Int. J. Environ. Res. Public Health 16 (7) (2019) 1121, https://doi.org/10.3390/ijerph16071121.
[21] L. Coppola, T. Bellezze, A. Belli, et al., Binders alternative to Portland cement and waste management for sustainable construction. Part 1, J. Appl. Biomater. Funct. Mater. 16 (3) (2018) 186–202, https://doi.org/10.1177/2280800018782845.
[22] L. Nguyen, A.J. Moseson, Y. Farnam, S. Spatari, Effects of composition and transportation logistics on environmental, energy and cost metrics for the production of alternative cementitious binders, J. Clean. Prod. 185 (2018) 628–645, https://doi.org/10.1016/j.jclepro.2018.03.120.
[23] ASTM C192/C192M, Standard Practice for Making and Curing Concrete Test Specimens in the Laboratory, ASTM International, 2024. www.astm.org.
[24] ASTM C469-C469M, (2022), "Standard test method for static modulus of elasticity and poisson's ratio of concrete in compression", ASTM International, PA, www.astm.org.
[25] ASTM C39, (2023), "Standard test method for compressive strength of cylindrical concrete specimens", ASTM International, www.astm.org.
[26] L. De Marchi, A. Marzani, M. Miniaci, A dispersion compensation procedure to extend pulse-echo defects location to irregular waveguides, NDT Int. 54 (2013) 115–122, https://doi.org/10.1016/j.ndteint.2012.12.009.
[27] M. Miniaci, A.S. Gliozzi, B. Morvan, A. Krushynska, F. Bosia, M. Scalerandi, N. M. Pugno, Proof of concept for an ultrasensitive technique to detect and localize sources of elastic nonlinearity using phononic crystals, Phys. Rev. Lett. 118 (21) (2017) 214301, https://doi.org/10.1103/PhysRevLett.118.214301.
[28] M. Miniaci, R.K. Pal, B. Morvan, M. Ruzzene, Experimental observation of topologically protected helical edge modes in patterned elastic plates, Phys. Rev. X. 8 (3) (2018), https://doi.org/10.1103/physrevx.8.031074.
[29] D. Briccola, M. Cuni, A. De Juli, M. Ortiz, A. Pandolfi, Experimental validation of the attenuation properties in the sonic range of metaconcrete containing two types of resonant inclusions, Exp. Mech. 61 (3) (2021) 515–532, https://doi.org/10.1007/s11340-020-00668-4.
[30] C. Xu, W. Chen, T.M. Pham, K. Bi, R. Cheng, H. Hao, Designing novel metaconcrete structures with low-frequency bandgap against dynamic loads, Structures 70 (2024) 107748, https://doi.org/10.1016/j.istruc.2024.107748.
[31] F. Greco, L. Leonetti, U. De Maio, S. Rudykh, A. Pranno, Macro- and micro-instabilities in incompressible bioinspired composite materials with nacre-like microstructure, Compos. Struct. 269 (2021) 114004, https://doi.org/10.1016/j.compstruct.2021.114004.